Effect of the density of states at the Fermi level on defect free energies and superconductivity: A case study of Nb₃Sn

Nathan S. Sitaraman [*], Michelle M. Kelley, Ryan D. Porter, Matthias U. Liepe, and Tomás A. Arias [†]
Department of Physics, Cornell University, Ithaca, New York 14853, USA

Jared Carlson, Alden R. Pack, and Mark K. Transtrum
Department of Physics and Astronomy, Brigham Young University, Provo, Utah 84602, USA

Ravishankar Sundararaman
Department of Materials Science and Engineering, Rensselaer Polytechnic Institute, Troy, New York 12180, USA

Although often ignored in first-principles studies of material behavior, electronic free energy can have a profound effect in systems with a high-temperature threshold for kinetics and a high Fermi-level density of states (DOS). Nb₃Sn and many other members of the technologically important A15 class of superconductors meet these criteria. This is no coincidence: both electronic free energy and superconducting transition temperature T_c are closely linked to the electronic density of states at the Fermi level. Antisite defects are known to have an adverse effect on T_c in these materials because they disrupt the high Fermi-level density of states. We observe that this also locally reduces electronic free energy, giving rise to large temperature-dependent terms in antisite defect formation and interaction free energies. This work explores the effect of electronic free energy on antisite defect behavior in the case of Nb₃Sn. Using *ab initio* techniques, we perform a comprehensive study of antisite defects in Nb₃Sn, and find that their effect on the Fermi-level DOS plays a key role determining their thermodynamic behavior, their interactions, and their effect on superconductivity. Based on our findings, we calculate the A15 region of the Nb-Sn phase diagram and show that the phase boundaries depend critically the electronic free energy of antisite defects. In particular, we show that extended defects such as grain boundaries alter the local phase diagram by suppressing electronic free-energy effects, explaining experimental measurements of grain boundary antisite defect segregation. Finally, we quantify the effect of antisite defects on superconductivity with the first *ab initio* study of T_c in Nb₃Sn as a function of composition, focusing on tin-rich compositions observed in segregation regions around grain boundaries. As tin-rich compositions are not observed in bulk, their properties cannot be directly measured experimentally; our calculations therefore enable quantitative Ginzburg-Landau simulations of grain boundary superconductivity in Nb₃Sn. We discuss the implications of these results for developing new growth processes to improve the properties of Nb₃Sn thin films.

I. INTRODUCTION

Finite-temperature density-functional theory (DFT) has long been possible, and is even preferable to zero-temperature DFT in the case of metals for reasons of computational efficiency [1,2]. However, for many systems, energies calculated in a zero-temperature approximation are satisfactory for all temperatures of interest, and vibrational and electronic free-energy contributions to the free energy constitute only small corrections to the zero-temperature energy [3,4]. The exceptions to this rule can be interesting: vibrational entropy plays a central role in the physics of shape-memory alloys, for example [5–9]. In this paper we consider the class of A15 superconductors, focusing on the case of Nb₃Sn where we

find that a very high Fermi-level density of states (DOS) lets electronic free energy play the starring role.

Metallic compounds of the A15 crystal structure are type-II superconductors, many of which have high critical temperatures in large part because of their high electronic densities of states at the Fermi level [10–12]. These materials exist in an interesting regime between elemental and high-T_c superconductors [10]. Their critical temperatures and upper critical fields (18 K and 30 T, respectively, in the case of Nb₃Sn) far exceed the limits of elemental superconductors, and they maintain these excellent properties in large, polycrystaline samples, unlike high-T_c superconductors [13–19]. As a result, A15 superconductors have long been the gold standard for superconducting wire applications [20–24], and Nb₃Sn films are a promising candidate material for superconducting radio-frequency (SRF) applications [25–31]. A point of difficulty in making these materials available for practical applications, however, is that their excellent superconducting properties are only achieved at compositions very close to the ideal 3:1

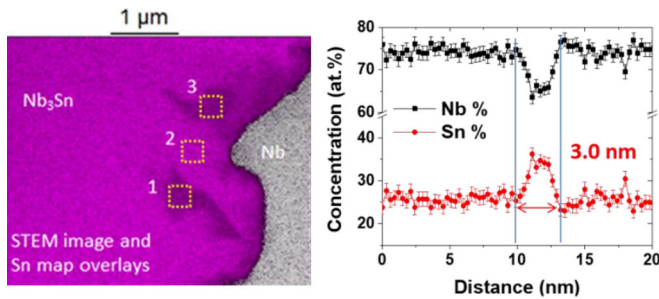[*]nss87@cornell.edu
[†]taa2@cornell.edu

FIG. 1. Left, atomic composition of a sample cross section showing regions of niobium segregation (1 and 3) in contrast to 25% tin regions (2), reproduced from [36] (Lee *et al.*). Right, atomic composition measured by atom-probe tomography near a grain boundary showing tin segregation; the 3-nm-wide segregation region is significantly wider than the region of structural disorder at the boundary core. Reproduced from [37] (Lee *et al.*).

composition [32,33]. When composition departs from the ideal, it is typically because of the presence of antisite defects, which disrupt the electronic structure of the material and degrade its superconducting properties.

In this work, we begin by showing that the strong effect of antisite defects on the Fermi-level DOS in Nb_3Sn not only explains their negative effect on T_c, but also explains their thermodynamic behavior by reducing electronic free energy. Based on these calculations, we provide an accurate theoretical explanation for antisite defect concentrations in the dilute limit of pristine Nb_3Sn in Sec. III. In Sec. IV, we extend our analysis to consider higher concentrations of antisite defects by accounting for their temperature-dependent interaction free energies, resulting in theories for the observed phase boundaries for the A15 Nb-Sn phase, and for observed antisite defect segregation at grain boundaries (Fig. 1). Then, in Sec. V, we present the first calculations of T_c as a function of composition in Nb_3Sn, including tin-rich compositions that cannot be probed directly by experiments. Our results quantify the effect of antisite defect segregation on T_c and enable Ginzburg-Landau simulations of magnetic flux entry at grain boundaries. Finally, in Appendices A and B, we discuss the practical implications of our findings for the optimization of Nb_3Sn film growth for SRF applications.

The importance of electronic free energy in the case of Nb_3Sn strongly suggests that it plays a significant role in the thermodynamics of antisite defects in other A15 materials, and in general in materials with strong coupling between composition and electronic free energy. This work builds on our previous results on the Nb-Sn phase diagram [34] and Nb_3Sn T_c [35].

II. METHODOLOGY

All calculations are performed within a density-functional theory plane-wave pseudopotential framework using the open-source plane-wave software JDFTX [38,39]. To treat electron exchange and correlation, we use the Perdew-Burke-Ernzerhof (PBE) version of the generalized gradient approximation [40] to the exact density functional. To represent the effects of the atomic cores we employ ultrasoft

TABLE I. A15 supercells for T_c vs composition calculations. Lattice vectors are measured in units of the cubic unit-cell lattice vector, and do not reflect small changes that occur during lattice relaxation as a result of defects or the small tetragonal distortion of pure Nb_3Sn. Angles are measured in degrees.

Atoms	a	b	c	α	β	γ
8	1	1	1	90	90	90
16	2	1	1	90	90	90
16	$\sqrt{2}$	$\sqrt{2}$	1	90	90	90
24	$\sqrt{3}$	$\sqrt{2}$	$\sqrt{2}$	120	90	90
64	2	2	2	90	90	90

pseudopotentials [41], leaving as valence electrons niobium $4p^6 5s^2 4d^3$ and tin $4d^{10} 5s^2 5p^2$. For total-energy calculations we use a 20-Hartree plane-wave cutoff energy in order to minimize Pulay effects on calculated energy differences resulting from changes in the plane-wave basis set during lattice minimization. Electron-phonon calculations involved in calculating T_c use a 12-Hartree plane-wave cutoff energy. To treat the metallic Fermi surface, all calculations employ a 4.5-milliHartree electron temperature, chosen to be close to the actual experimental growth temperature for Nb_3Sn films of about 1420 K. For zero-temperature properties, we use the cold-smearing method developed by Marzari [42] with the same 4.5-milliHartree smearing width in order to ensure that zero-temperature energies are converged to the same tolerance as high-temperature energies with respect to k-point sampling. For total-energy calculations on the A15 phase, we use a 64-atom supercell, and a $4 \times 4 \times 4$ k-point mesh to sample the Brillouin zone of the supercell. For the Nb_6Sn_5 phase, we use the 44-atom unit cell, and a $3 \times 6 \times 9$ k-point mesh. For the bcc phase, we use a 54-atom supercell, and a $5 \times 5 \times 5$ k-point mesh.

To calculate T_c as a function of composition, we consider *all possible* unique antisite defects in (a) the 8-atom Nb_3Sn unit cell, (b) two different tetragonal 16-atom supercells, (c) one right rhombic 24-atom supercell, and (d) the cubic 64-atom supercell. These supercells are described in detail in Table I. Turning now to our phonon calculations, for the 8-atom cell and the ($a = 2$) 16-atom cell, we use a 64-atom supercell with a $2 \times 2 \times 2$ k-point mesh. For the other 16-atom cell, we use a 128-atom supercell with a $2 \times 2 \times 2$ k-point mesh. For the 24-atom cell, we use a 96-atom supercell with a $2 \times 2 \times 3$ k-point mesh. And for the 64-atom cell, we use the unit cell with a $2 \times 2 \times 2$ k-point mesh.

III. NONINTERACTING UNPAIRED ANTISITE DEFECTS

Antisite defects are the most common point defects in Nb_3Sn, with formation energies much lower than either species of vacancy [43]. Therefore, when Nb_3Sn is close to ideal stoichiometry, the system can be modeled as perfect Nb_3Sn containing dilute antisite defects [44]. This is the case for the bulk of Nb_3Sn superconductors grown with modern techniques; for example, the experimental data in Fig. 1 for Nb_3Sn thin films grown by vapor deposition shows only small compositional deviations outside of the prominent segregation

TABLE II. Antisite defect formation energies and free energies [including electronic free energy but neglecting vibrational free energy (see text)] in stoichiometric Nb_3Sn.

Defect	0 K energy	1420 K free energy	Difference
Nb_{Sn}	0.31 eV	0.47 eV	+0.16 eV
Sn_{Nb}	0.31 eV	0.60 eV	+0.29 eV
Pair	0.62 eV	1.07 eV	+0.45 eV

regions, and Nb_3Sn wires produced through the bronze route are similarly homogeneous [45].

To calculate antisite defect concentration in stoichiometric Nb_3Sn, we begin by considering the antisite defect pair formation free energy in the noninteracting approximation, i.e., assuming that the pair formation free energy is determined by the free energies for single isolated antisite defects. Because there is no strong attractive interaction between antisite defects in Nb_3Sn (see Sec. IV), the noninteracting approximation is valid for near-stoichimetric Nb_3Sn, where antisite defects are dilute. Specifically, we estimate that accounting for interactions would affect our estimated fractional antisite defect concentration in stoichiometric Nb_3Sn by less than 0.002 at temperatures under 2000 K.

In this work, we will use Nb_{Sn} and Sn_{Nb} to refer to the two different antisite defects, niobium atoms occupying tin sites, and tin atoms occupying niobium sites, respectively. In the noninteracting approximation, the deviation x from perfect stoichiometry can be expressed as

$$x = \frac{1}{4}\exp\left(-F_{Nb_{Sn}}/kT\right) - \frac{3}{4}\exp\left(-F_{Sn_{Nb}}/kT\right). \quad (1)$$

Table II shows the calculated formation free energies $F_{Nb_{Sn}}$, $F_{Sn_{Nb}}$, and $F_{Nb_{Sn}} + F_{Sn_{Nb}}$ for antisite defects in stoichiometric Nb_3Sn ($x = 0$), both at 0 and at 1420 K, a typical growth temperature for Nb_3Sn thin films [27]. We find that the pair formation free energy at 1420 K is nearly twice the pair formation energy at 0 K, increasing by 0.45 eV, a difference attributable to the decrease in electronic free energy associated with the defect pair. Antisite defects reduce electronic free energy by reducing the Fermi-level DOS. The Fermi-level DOS is highly sensitive to defects because of the narrow density-of-states peak that appears at the Fermi level in the undefected material (Fig. 2). This peak is easily flattened by disorder.

Vibrational free energy constitutes an additional correction to the pair formation free energy, which is linear in temperature at high temperatures [46]. Our preliminary calculations indicate that vibrational free energy adds an additional ∼0.08 eV to the pair formation free energy at 1420 K, about a factor of 6 smaller than the electronic free-energy contribution. However, we note that this estimate is fairly uncertain because of the sensitivity of vibrational free-energy differences to small changes in the phonon dispersion, a subtle topic in the case of Nb_3Sn [47]. Because of the preliminary nature of these vibrational free-energy calculations and the relatively small magnitude of the correction, this contribution is not included in the free energies reported in Table II.

Having calculated antisite defect free energies at 0 and 1420 K, we are now in position to determine their free
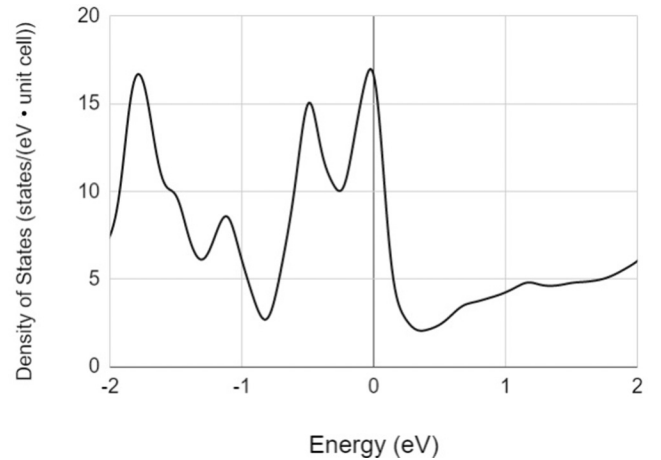

FIG. 2. Density of states versus energy difference from Fermi level in pure Nb_3Sn. The high peak at the Fermi level plays a crucial role in determining defect and superconducting behaviors.

energies as functions of temperature. In general, the electronic free energy amounts to a convolution between the electronic DOS and the Fermi distribution; the standard result, to first approximation, is

$$F_{elec} = E_{elec} - TS_{elec} = E_{elec} - n(0)(\pi^2)(kT)^2/6, \quad (2)$$

where $n(0)$ is the Fermi-level DOS. We therefore express the temperature-dependent defect formation free energy as $F = E - T(\alpha T)$, where E is the zero-temperature formation energy, and the temperature-dependent electronic entropy αT is proportional to the effect $\delta n(0)$ of the defect on the Fermi-level DOS. We calculate E and α for antisite defects based on our results in Table II. To this free energy, we then add the configurational entropy contribution $-TS_{config}(c)$ for the collection of defects and minimize with respect to defect concentration to determine the equilibrium antisite defect concentration in near-stoichiometric Nb_3Sn as a function of temperature (Fig. 3).

We find that, before accounting for electronic free-energy effects, the predicted fractional antisite defect concentration is both very high, quickly rising by several atomic percent beyond 1000 K, and strongly temperature dependent. With proper accounting for electronic free energy, however, the predicted antisite defect concentration is much lower, and only weakly temperature dependent at high temperatures. At 25% tin composition, it remains under 0.01 until about 1300 K, and has a maximum of about 0.012. This unusual behavior results from the quadratic electronic free-energy term in the defect formation free energy.

The estimated defect concentration is in reasonably good agreement with recent measurements by Flukiger *et al.*, which found antisite defect concentrations of 0.005 ± 0.002 in Nb_3Sn, much lower than in other A15 compounds such as Nb_3Al (0.04 ± 0.02) [44,48]. The discrepancy between our estimate and the measured value corresponds to an error of about 0.1 eV in the pair formation free energy, which could be the result of an unaccounted for vibrational free-energy contribution. We note that an antisite defect concentration of 0.01 is not sufficiently high to significantly affect the electronic
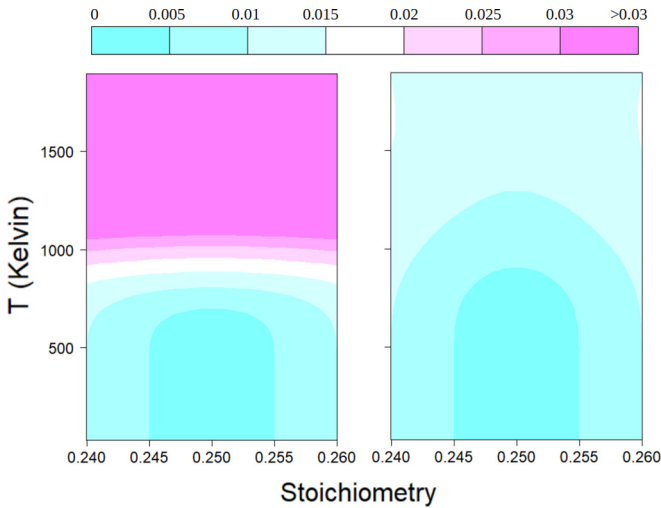
FIG. 3. Fractional antisite defect concentration as a function of composition and temperature, calculated without (left) and with (right) electronic free-energy effects. Contours are at intervals of 0.005, with concentrations beyond 0.03 in dark pink.

structure of Nb$_3$Sn, but it likely sets the electron mean-free path and, in general, may play a role in determining the amplitudes of important scattering processes. This is in contrast to the case of elemental superconductors such as niobium, in which the electron mean-free path is determined by interstitial impurity concentrations.

The effect of antisite defects on the Fermi-level DOS not only determines the equilibrium defect concentration, but also determines how these defects interact with each other and with other defects. Defects that suppress the Fermi-level DOS in some volume of radius R (visualized in Fig. 4) reduce the amount by which other defects can suppress the electronic free energy when present in the same region. Because the electronic free energy of defect formation is directly related to the extent to which a defect suppresses the Fermi-level DOS, we expect to find a significant entropy-mediated attractive interaction between defects that reduce the Fermi-level DOS.
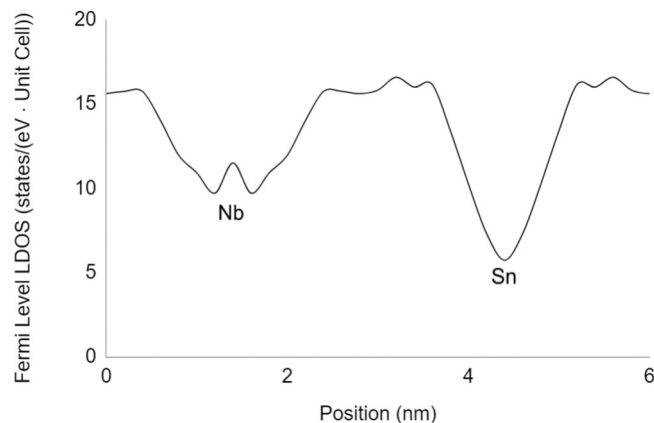

FIG. 4. Change in local density of states (LDOS) at the Fermi level versus position in a $1 \times 1 \times 12$ supercell with a Nb$_{Sn}$ defect at $\sim$1.8 nm and a Sn$_{Nb}$ defect at $\sim$4.2 nm. Both antisite defects affect the Fermi-level LDOS in a radius of just under 1 nm.

One result of this attractive electronic free-energy effect is that interactions between antisite defects, which are strongly repulsive at low temperatures, become only mildly repulsive at high temperatures. Understanding the temperature dependence of these interactions is crucial to accurately calculating the stoichiometry limits of the A15 phase at high temperatures. Another implication of this electronic free-energy effect is that antisite defects are attracted at elevated temperatures to regions near grain boundaries and dislocations, where the Fermi-level DOS is lower because of disorder and strain [12]. We investigate these phenomena quantitatively in the following section.

IV. INTERACTING ANTISITE DEFECTS: PHASE DIAGRAM AND GRAIN BOUNDARIES

In the previous section we investigated the properties of antisite defects in the dilute limit; here we extend our analysis to understand their behavior over the wide range of experimentally observed concentrations. Nb$_3$Sn represents a specific composition of the A15 Nb-Sn phase, which extends from about 17.5% to about 26% tin content in the experimentally established phase diagram [49]. Tin-poor composition is the result of high concentrations of Nb$_{Sn}$ defects, and is known to greatly suppress superconducting properties; experimentally, this is observed in sharply defined regions in some samples (Fig. 1) [36,50,51]. The same degree of tin-rich composition, the result of high concentrations of Sn$_{Nb}$ defects, is never observed in bulk samples, but is observed in regions around grain boundaries. The $\sim$3-nm width of these regions and large interfacial excess of up to 20 atoms nm^{-2} are not consistent with simple Langmuir-McLean model grain boundary core segregation, so a careful investigation is warranted [52]. To understand both tin-poor and tin-rich phenomena, and in particular to determine if the observed defect segregation is better explained by kinetics or by thermodynamics, we calculate the A15 region of the Nb-Sn phase diagram from first principles.

In outline, our procedure to determine the phase diagram is as follows (details and justification in the following subsection). In order to generalize the analysis of Sec. III to higher defect concentrations, we calculate antisite defect pair interaction free energies. These calculations indicate that we can model the A15 free energy as the sum of the Sn sublattice free energy, for which we use the Monte Carlo method with pairwise interactions for Nb$_{Sn}$ defects, and the Nb sublattice free energy, for which we use a noninteracting Boltzmann factor approximation for Sn$_{Nb}$ defects because of their lower concentration. With this model we estimate equilibrium concentrations of the two species of antisite defects and the sublattice free energies as functions of Nb-Sn relative chemical potential. Then, we take the resulting free energy versus composition data and use the common-tangent convex hull approach to the Maxwell construction to determine the boundaries of the A15 phase and the competing bcc and Nb$_6$Sn$_5$ phases.

A. Methodology

To model interactions between defects, we employ a cluster expansion at the pair-interaction level. Specifically, we consider all possible antisite defect pair interactions:

TABLE III. Antisite pair interaction Gibbs free energies (including electronic free energy) at zero temperature and typical Nb_3Sn growth temperature. Positive values indicate repulsive interactions.

Interaction	0 K energy	1420 K free energy
Nb_{Sn}-Nb_{Sn}		
Nearest neighbor	0.17 eV	0.10 eV
2nd-nearest neighbor	0.09 eV	0.07 eV
3rd-nearest neighbor	0.02 eV	0.01 eV
Nb_{Sn}-Sn_{Nb}		
Nearest neighbor	−0.03 eV	−0.11 eV
2nd-nearest neighbor	0.16 eV	0.12 eV
3rd-nearest neighbor	0.06 eV	0.03 eV
Sn_{Nb}-Sn_{Nb}		
Nearest neighbor	0.61 eV	0.50 eV
2nd-nearest neighbor	0.07 eV	−0.02 eV
3rd-nearest neighbor	0.23 eV	0.18 eV

Nb_{Sn}-Nb_{Sn}, Nb_{Sn}-Sn_{Nb}, and Sn_{Nb}-Sn_{Nb}. We propose a realistic model simplified by neglecting interactions that satisfy the following specific criteria, which ensure that the neglected interactions will have negligible effects on the calculated phase diagram. First, the interactions must be weak or repulsive, so that bound defect pairs are not a consideration. Bound defect pairs can be neglected if their total formation free energy is significantly larger than the formation energy of the lowest-energy individual defect: $F_{pair} - F_{individual} \gg kT$, ensuring that the concentration of bound defect pairs is relatively small, $c_{pair} \ll c_{individual}$. Second, the defects involved in the pair must be dilute or, more precisely, the product of their concentrations must be small so that the concentration of coincidental pairs is likewise small. These criteria ensure that the concentration of interacting pairs is small enough that their impact on the overall energy per atom is negligible and therefore does not affect the convex hull or phase diagram.

Based on these criteria and our interaction energy calculations (Table III), we neglect Nb_{Sn}-Sn_{Nb} and Sn_{Nb}-Sn_{Nb} interactions. Therefore, we can express the total free energy as the sum of separate niobium and tin sublattice contributions. Furthermore, for the niobium sublattice, we can describe the concentration of Sn_{Nb} defects with a simple Boltzmann factor approximation. On the other hand, we determine that the Nb_{Sn}-Nb_{Sn} interaction is important and thus include these interactions at the nearest-, next-nearest-, and next-next-nearest-neighbor level within in our model. We then use the Metropolis Monte Carlo method to determine the Nb_{Sn} defect concentration as a function of temperature and Nb-Sn relative chemical potential. Metropolis-Hastings Monte Carlo calculations were performed on a periodic $8 \times 8 \times 8$ super-cell of the cubic eight-atom A15 unit cell, choosing sites at random and flipping occupancy state according to the Boltzmann acceptance criterion. Finally, we use a thermodynamic integration method to calculate the configurational entropy, allowing us to compute the free energy per atom as a function of temperature and composition which we use for our convex hull calculations.

For the common-tangent convex hull calculations, we consider the bcc niobium phase with tin substitutional defects
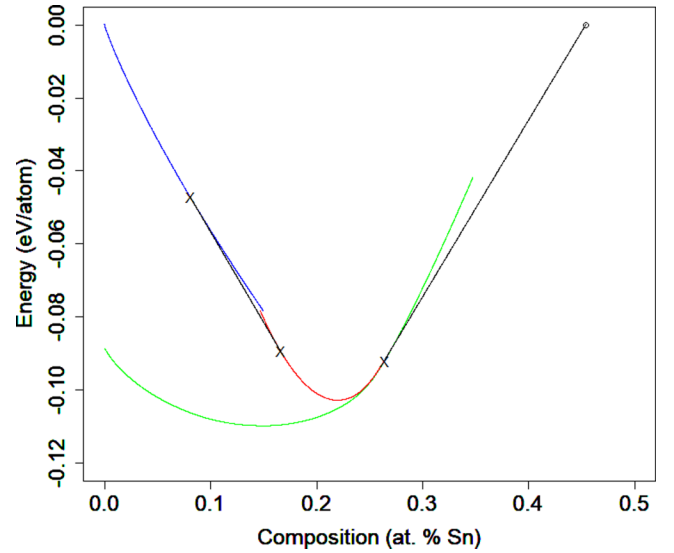

FIG. 5. Convex hull construction of free energy versus tin content at $T = 1100$ K: bcc phase (blue), A15 phase without (green) and with (red) Nb_{Sn}-Nb_{Sn} interactions, linear tangents (black), compositional limits of phases (×'s). The noninteracting approximation increasingly underestimates the A15 free energy at increasingly tin-poor compositions. The strong curvature of the A15 hull indicates that this phase favors compositional homogeneity in equilibrium.

and the Nb_6Sn_5 phase as the competing phases on the tin-poor and tin-rich A15 boundaries, respectively (Fig. 5). Our calculations find that vacancy and antisite defect energies in Nb_6Sn_5 are large compared to thermal energies of interest; therefore, we take it to be a defect free line compound as is observed experimentally. While Nb_6Sn_5 is experimentally observed only below temperatures of about 1200 K, we use it as a reference at all temperatures because of the difficulty in precisely calculating the free energy of the liquid solution that competes with the A15 phase at higher temperatures. Therefore, our calculated tin-rich A15 phase limit should be considered an upper bound for the true limit at temperatures above 1200 K.

B. Results

We find that our convex hull results at all temperatures exhibit some of the same key features that we see in Fig. 5. Specifically, we see that the A15 convex hull calculated by our Monte Carlo model is in agreement with the convex hull calculated using the noninteracting approximation described in Sec. III for compositions near 25% tin, but diverges quickly at tin-poor compositions. The Monte Carlo convex hull is characteristically smooth and convex, with nearly temperature-independent boundaries at $16.5 \pm 1.5\%$ and $26.5 \pm 1.5\%$ tin content. This is in agreement with the experimental phase diagram, which shows a single phase that varies continuously in composition from about 17.5% to about 26% tin content. Figure 6 displays our calculated temperature-concentration phase diagram for the A15 region of the Nb-Sn system, for the case of a DFT uncertainty of ± 2 meV/atom in energy differences for our convex hulls.
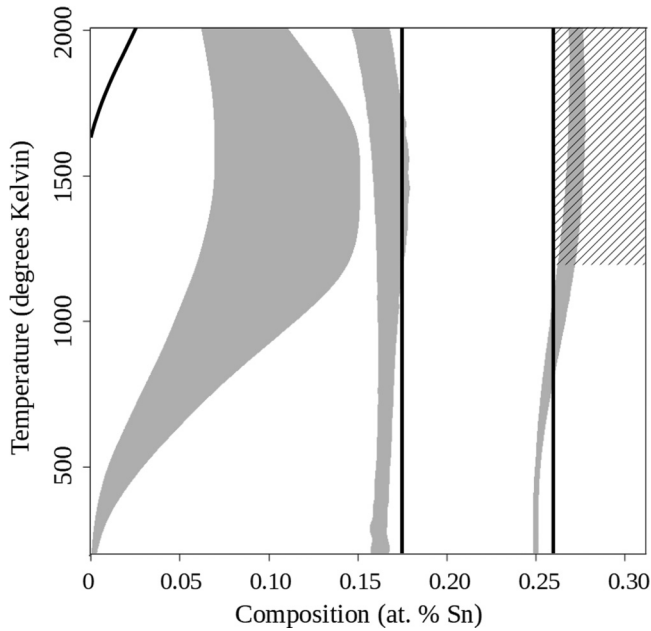
FIG. 6. Nb-Sn phase diagram: this work (shaded regions reflect estimated DFT uncertainties in phase boundaries), and experiment [49] (solid curves). Hash marks indicate the region where the Nb_6Sn_5 phase considered in this work is unstable experimentally (see text).

C. Discussion on the calculated phase boundaries

We find the tin-rich limit of the A15 phase to rise smoothly from 25% at low temperatures to a maximum of about 27% at high temperatures. The low-temperature limit of our calculation for this phase boundary is of high confidence; therefore, we propose a minor adjustment to established phase diagram: instead of a temperature-independent tin-rich phase limit of 26% [49], the tin-rich limit should smoothly approach 25% at low temperatures. Our result for the tin-rich limit at higher temperatures is somewhat higher than experimentally observed. This is due in part to our use of Nb_6Sn_5 as the competing phase at high temperatures, when in reality it is known that the Sn-Nb liquid solution phase has a lower free energy beyond about 1200 K. Accounting for the Sn-Nb liquid phase would lower our calculated tin-rich phase limit, bringing it in closer agreement with experimental values, but is unlikely to alter our qualitative understanding of the system. Such liquid-phase calculations would be a significant undertaking beyond the scope of this work. We expect that accounting for Sn_{Nb}-Sn_{Nb} interactions, which our calculations show are in most cases repulsive, would also lower our calculated tin-rich phase limit slightly.

For the tin-poor limit of the A15 phase, our results lie in the 15%–18% range at all temperatures, in good agreement with most experimental studies. As might be expected, our Monte Carlo simulations find that Nb_{Sn} defects begin to fall into low-energy superlattice configurations at sufficiently low temperatures. Triplet interactions and other corrections to our Monte Carlo model may be necessary in order to make an accurate determination of the minimum-energy superlattice configuration for Nb_{Sn} defects. However, our calculated tin-poor phase boundary is not particularly sensitive to energy errors at low temperatures, and we find no evidence for the

narrowing of the compositional range at low temperatures suggested by some researchers [53,54]. Experimental investigations of the phase diagram at low temperatures have so far been limited by the extremely slow kinetics of diffusion in the A15 Nb-Sn phase below about 800 K [43].

Between the tin-rich and tin-poor limits, we find that the A15 hull is smooth and convex (Fig. 5). This means that the phase tends towards compositional homogeneity or, equivalently, that Nb_{Sn} defect segregation is not thermodynamically favorable. This is because there is a net repulsive interaction between Nb_{Sn} defects, as even at high temperatures the repulsive strain component of the interaction is larger than the attractive electronic free-energy component of the interaction. This supports the established phase diagram which shows a single A15 phase, as opposed to distinct stoichiometric and tin-poor A15 phases. We therefore conclude that experimentally observed Nb_{Sn} segregation regions in Nb_3Sn thin-film samples grown using the vapor deposition process are likely the result of a kinetic mechanism; such a mechanism is proposed and discussed in detail in Appendix A.

The tin solubility limit of the bcc niobium phase is quite uncertain experimentally, with most measurements below $\sim$1500 K finding no more than $\sim$1% solubility, but at least one indirect measurement finding much higher solubility on the order of 10% [55]. Our calculation is tentatively in agreement with the latter, suggesting that the phase boundary passes 1% tin by 500 K, and increases to a maximum on the order of 10% near 1500 K. It is possible that some experiments failed to access the phase boundary because of the slow kinetics of tin diffusion in niobium and Nb_3Sn. Results from self-diffusion studies of niobium [56] indicate that it would take more than a day to achieve self-diffusion across 100 nm at 1400 K, or about a month to achieve self-diffusion across 100 nm at 1300 K. Alternatively, it is possible that the absence of a vibrational term in the free energy results in an error in the calculated tin solubility in bcc niobium. Our preliminary calculations indicate that tin substitutional defects in niobium have a small positive vibrational free energy of about $\approx$0.03 eV at the coating temperature; accounting for this would result in a slightly lower predicted solubility limit for tin in niobium. We note that the calculated tin-rich limit of the bcc phase is much more sensitive to uncertainties in our energy calculations than are our A15 phase limits.

D. Effect of grain boundaries on the calculated phase boundaries

Here we address the question of why some grain boundaries have compositions beyond the tin-rich limit of the bulk phase diagram. The bulk phase diagram's tin-rich limit of 25% at low temperatures rises exponentially at intermediate temperatures, but this is halted at higher temperatures by the rising electronic free energy of Sn_{Nb} defects. We propose a simple model that shows why the tin-rich limit of the phase continues to rise with increasing temperature in the vicinity of grain boundaries, explaining the high tin concentrations measured experimentally in these regions [37,57].

Our model assumes the Fermi-level DOS is reduced because of disorder and strain in a region around the grain boundary. Density-functional theory calculations have
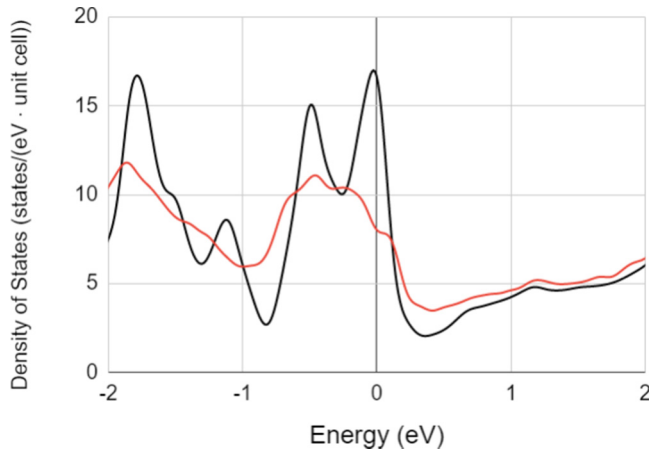
FIG. 7. Density of states versus energy difference from Fermi level in pure Nb_3Sn (black) and in a grain boundary calculation (red) [59].

FIG. 9. Phonon spectral function $\alpha^2 F$ versus energy in A15 Nb-Sn: 25% tin content (black), 26.6% (dark red), 29.2% (red), 31.3% (light red). $\alpha^2 F$ decreases with increasing tin content above 25% across all energies.

quantified this reduction in the DOS for one grain boundary structure analyzed in an unpublished thesis [58]. Our own analysis of this structure confirms their finding (Fig. 7), and further analysis of different structures shows that the magnitude of this effect seems to be independent of grain boundary type [59]. We then assume that, as a result of the lower Fermi-level DOS, the strong temperature dependence of antisite defect formation free energies is also reduced in this region, bringing antisite defect formation free energies closer to the 0-K values in Table II. Lower antisite defect formation free energies would allow the A15 phase to reach higher tin compositions in the region around the grain boundary, as is seen experimentally.

We find that that a sufficiently large reduction in the electronic free-energy contribution to the antisite defect formation energies would allow the tin-rich limit of the A15 phase to extend beyond 30% tin (Fig. 8), to concentrations similar to those seen experimentally near grain boundaries. Our
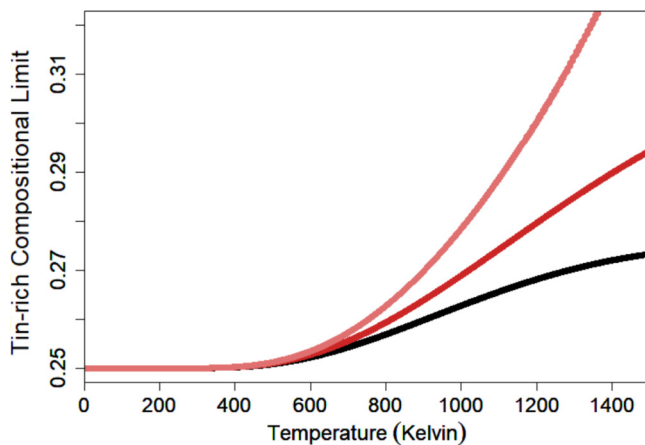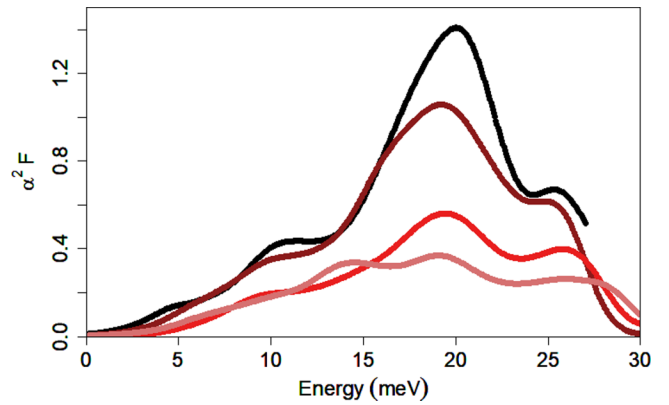

FIG. 8. Predicted tin-rich phase limit of A15 Nb-Sn versus temperature: expected bulk dependence (black), dependence in regions where the electronic free-energy contribution to the antisite defect formation free energy is reduced by 25% (dark red) and 50% (light red).

recent atomistic grain boundary calculations provide evidence that Sn_{Nb} antisite defects indeed have lower free energies at sites near grain boundaries [59]. In particular, the electronic free-energy contribution to the defect formation free energy is completely suppressed in the grain boundary core, and is suppressed by more than 10% out to distances of more than 1 nm from the grain boundary. An in-depth investigation of the equilibrium spatial distribution of antisite defects around a grain boundary is beyond the scope of this work, but we note that it is possible to perform such a calculation using a standard model for grain boundary segregation, given the distribution of lower free-energy sites and our calculated Sn_{Nb}-Sn_{Nb} pair interaction free energies [60].

V. T_c VERSUS STOICHIOMETRY

The critical temperature of A15 Nb-Sn has been studied experimentally, with the conclusion that T_c has a maximum value of about 18 K near the 25% tin stoichiometry of Nb_3Sn, and a minimum value of about 6 K at the tin-poor limit of 17%–18% tin [54,61]. However, the superconducting properties of tin-rich compositions beyond 26% tin, which have been observed near grain boundaries, have not been measured [37,57]. Motivated to understand the effect of these tin-rich grain boundaries on Nb_3Sn superconductivity, we present the results of the first *ab initio* calculations of T_c as a function of composition in A15 Nb-Sn, and we show that, here too, the defect sensitivity of the Fermi-level DOS plays a central role in determining material properties.

We use Eliashberg theory [62] for strong-coupled superconductors within a DFT framework to determine T_c, calculating electron-phonon matrix elements and employing Wannier function methods to integrate smoothly over all scattering processes on a dense momentum-space grid in order to precisely determine scattering rates [63–66]. These scattering amplitudes are used to calculate the phonon spectral function (Fig. 9), which we then use to estimate T_c using the McMillan formula [67]. We repeat this process for different A15 supercells (see Sec. II) with compositions across the experimentally observed range to find the compositional dependence of T_c.
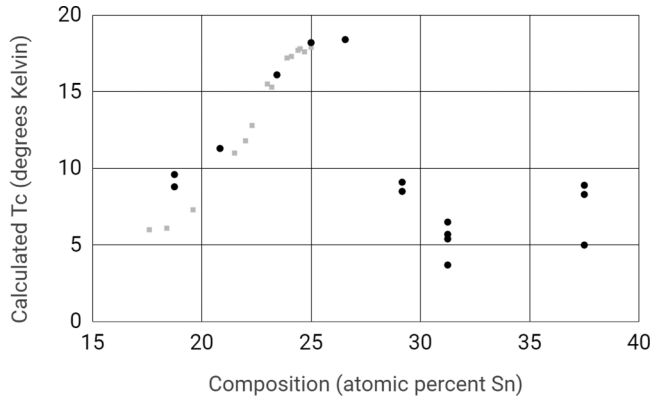
FIG. 10. Superconducting transition temperature T_c versus tin content of A15 Nb-Sn: experiment [54,61,68] (gray squares) and this work (black circles). We predict T_c to reach a minimum of about 5 K near 31% tin content in the tin-rich regime. Multiple data points at the same composition represent calculations for supercells with different antisite defect configurations.
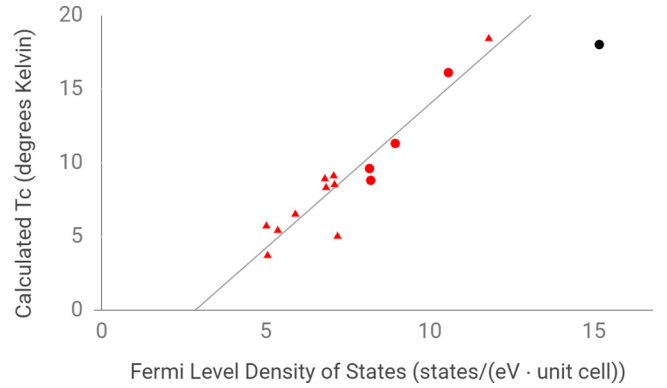

FIG. 11. Predicted T_c versus Fermi-level density of states in A15 Nb-Sn of varying composition: tin-poor compositions (red circles), tin-rich compositions (red triangles), Nb_3Sn stoichiometry (black circle). The data illustrate a nearly linear relationship for off-stoichiometery calculations.

A previous first-principles study of Nb_3Sn by Mentink *et al.* [11] explores the effect of electron-lifetime broadening on superconducting properties and finds that greater electron-lifetime broadening results in a lower Fermi-level DOS and a lower T_c. Following Mentink *et al.*, we use a constant effective Coulomb repulsion term $\mu^* = 0.125$ and apply a fixed broadening energy of 0.01 and 0.0012 eV to the electronic states and phonon states, respectively. We choose the broadening energy for electronic states to be consistent with the low normal-state resistivity of Nb_3Sn, and note that it is on the lower end of the range explored by Mentink *et al.*

Figure 10 compares our calculated superconducting transition temperature T_c as a function of tin content with observed experimental values. We find excellent agreement with experiment for calculations near 25% tin. For tin-rich compositions, which are not easily accessed experimentally, we find that T_c falls to a minimum of about 5 K at 31.25% tin. For tin-poor compositions, we calculate a minimum T_c of about 9 K at 18.75% tin, modestly above the experimentally measured minimum value (Table IV). This discrepancy may arise from our use of a fixed broadening energy for all calculations when tin-poor samples are likely to be highly disordered, making a larger broadening energy more appropriate. The results of Mentink *et al.* suggest that this adjustment would indeed likely lead to lower calculated T_c values [11].

We now apply our results on the superconductivity of A15 Nb-Sn as a function of composition to build a realistic model

of grain boundary superconductivity in Nb_3Sn, accounting for both variations in composition and for structural disorder in the boundary core. To quantify the impact of structural disorder, we take advantage of the strong correlation between our calculated T_c and the Fermi-level DOS in our compositional study, shown in Fig. 11. This relationship is an important tool as it provides an alternative to preforming full Eliashberg theory calculations, which become computationally prohibitive for complex defects such as grain boundaries. Our atomistic study of grain boundaries in Nb_3Sn [59] provides a comprehensive account of this work.

Combining our first-principles T_c calculations, first-principles grain boundary calculations [59], and experimental measurements of the compositional profile around grain boundaries [37], we have enabled Ginzburg-Landau simulations of magnetic flux entry at grain boundaries (Fig. 12) in the case of a superconducting surface exposed to an AC electromagnetic field [69]. These simulations spotlight the important relationship between the width of the tin segregation region and the superconducting coherence length of Nb_3Sn: tin-rich grain boundaries with widths approaching the coherence length can admit flux even at modest fields, a serious concern for SRF cavity applications [69–73]. Likewise, grain boundary segregation on a similar length scale in the
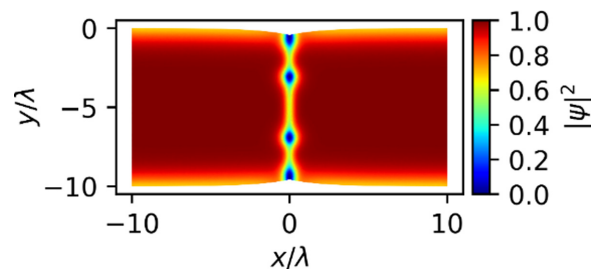
TABLE IV. Comparison of calculated and experimentally measured values for superconducting transition temperature T_c in the tin-poor regime. The dagger denotes averaged over two configurations.

Composition	Experimental T_c (K) [61]	Calculated T_c (K)
18.75% Sn	6	9.2[†]
20.83% Sn	9.5	11.3
23.44% Sn	16	16.1
Nb_3Sn	18	18.2

FIG. 12. Map of the square of the superconducting order parameter $|\psi|^2$ in a Nb_3Sn layer cross section with a tin-rich grain boundary (center), adapted from [69]. Distances are measured in units of the RF penetration depth $\lambda \approx 100$ nm.

Nb-Sn-Cu ternary system appears to have an important effect on flux pinning in Nb$_3$Sn wires [57,74,75].

VI. CONCLUSIONS

Our density-functional theory study of Nb$_3$Sn provides a clear and pertinent example of the key role electronic free energy plays in the thermodynamics of certain systems. In particular, the negative effect of antisite defects on this material's Fermi-level DOS reduces electronic free energy, and we show that this has important implications for defect behavior at high temperatures. Accounting for this effect, we provide an accurate theoretical explanation for antisite defect concentrations in the dilute limit, for the observed phase boundaries for the A15 Nb-Sn phase, and for observed antisite defect segregation at grain boundaries (Fig. 1). We further present the first *ab initio* calculations of T_c as a function of composition in Nb$_3$Sn, including tin-rich compositions, the superconducting properties of which cannot directly be measured. These calculations enable Ginzburg-Landau simulations of magnetic flux behavior at tin-rich grain boundaries, which is crucial for practical applications. Taken together, these results help to build a complete picture from first principles of how antisite defects form and segregate during material growth, and how they ultimately impact superconducting behavior.

The methods and insights in this paper should also apply directly to other members of the class of A15 superconductors. The difficulty in making these materials available for practical applications stems almost entirely from the challenge of limiting antisite defect concentrations, as these defects destroy the sharp DOS peak at the Fermi level and thus degrade the superconducting properties. For example, Nb$_3$Ge has a T_c of 23 K, even higher than that of Nb$_3$Sn, but this is reduced to 7 K by antisite disorder except in specially prepared metastable samples [10]. Our results show that understanding the effect of antisite defects on electronic free energy is crucial to building realistic models for their thermodynamic behavior during material growth. In general, we expect that when strong coupling exists between composition and electronic free energy in a material, its thermodynamics will be affected by this electronic free energy. Further research along these lines will improve our understanding of these materials, which we might refer to as "dynamic entropy" materials. This will aid ongoing efforts to optimize them for superconducting and other applications.

APPENDIX A: ON THE FORMATION OF TIN-POOR REGIONS IN Nb$_3$Sn DURING VAPOR DEPOSITION GROWTH

The insights gained from our theoretical study of antisite defects have important practical applications, for example, in
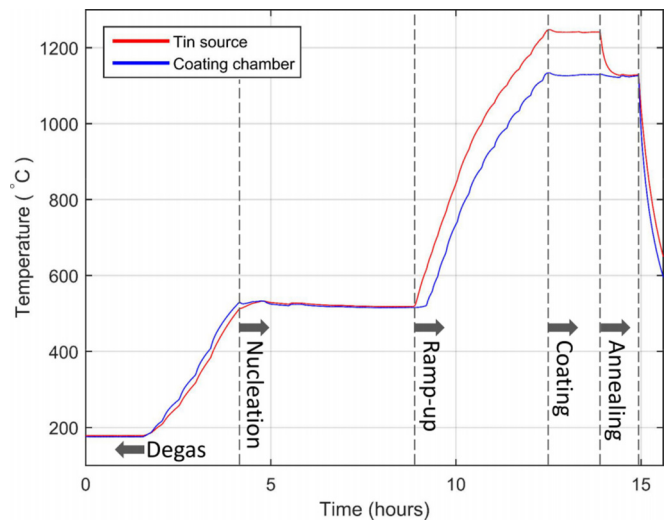

FIG. 13. The Cornell coating recipe [27]. The annotated steps are described in the text.

optimizing the vapor growth process for Nb$_3$Sn thin films for SRF applications. Specifically, our calculations predict that the A15 phase should not tend to phase separate into stoichiometric and tin-poor regions, improving our understanding of the experimentally observed tin-poor regions in Nb$_3$Sn thin films grown by vapor deposition. We conclude that the observed inhomogeneities in composition are likely attributable to kinetic phenomena, not to equilibrium phase separation. Barring some as-yet unaccounted factor, such as stress fields that might make sharp compositional variations within Nb$_3$Sn samples thermodynamically favorable, their presence requires the following: (a) the diffusion of tin within the A15 phase must be extremely slow at the growth temperature and (b) the chemical potential must change abruptly at certain times during layer growth.

The slow diffusion of tin in the A15 phase has been described in detail in a first-principles study [43]. To summarize, the activation energy for diffusion on tin sites is the sum of the niobium vacancy formation energy, the niobium vacancy hopping energy, and the Sn$_{Nb}$ defect formation energy, a quantity of about 3.5 eV. This high estimated activation energy is consistent with a very low diffusion rate. We therefore hypothesize that the composition of an A15 crystal is essentially static at typical growth temperatures, except in regions within nanometers of a diffusion pathway, such as an interface or a grain boundary.

To explain the abrupt changes in chemical potential, we briefly review the Nb$_3$Sn vapor deposition growth procedure (Fig. 13) [27]. Growth begins during the nucleation stage, when the tin chloride nucleation agent evaporates from the source and provides an initial supply of tin to the surface of the niobium cavity. Reaction rates are slow at the nucleation temperature of 500 °C, so only a very thin layer of Nb-Sn intermetallics begins to form. During the temperature rampup, reaction rates quickly increase, and above 930 °C the tin-rich intermetallics spontaneously decompose into Sn and Nb$_3$Sn, contributing to the layer growth. After this time, growth continues via a diffusion process in which tin travels
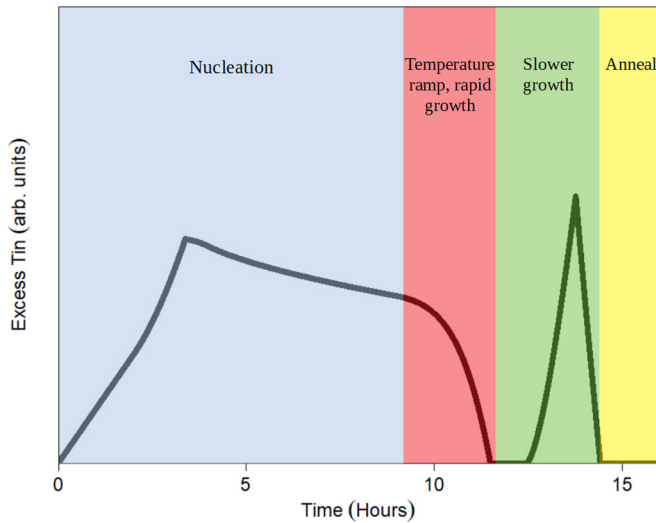
FIG. 14. Excess surface tin versus time for the Cornell coating recipe modeled using the temperature-dependent evaporation rates of tin and tin chloride [76] and the thickness-dependent growth rate [31] of the Nb_3Sn layer. Tin-poor growth is expected when there is no excess surface tin ($\sim$12 h and $\sim$15 h in this case).

through Nb_3Sn grain boundaries to react with niobium at the Nb-Nb_3Sn interface [36]. By the time the coating stage is reached, grain size increases and growth rate decreases in proportion to the decreasing concentration of grain boundary diffusion pathways [31]. Finally, during the annealing stage, the tin supply is exhausted, halting the growth process before the cavity begins cooling down.

We hypothesize that there are two distinct growth states for the Nb_3Sn layer during vapor diffusion growth. In the tin-rich growth state, tin vapor arrives on the surface at a faster rate than it is consumed in the Nb_3Sn formation reaction, resulting in the accumulation of a layer of liquid tin on the surface and a high chemical potential for tin on the surface. We posit that this high tin chemical potential is carried through to the Nb-Nb_3Sn interface by fast grain boundary diffusion, which thus enables Nb_3Sn growth at a composition near the tin-rich limit. In the tin-poor growth state, tin vapor arrives on the surface at a slower rate than it is consumed in the Nb_3Sn formation reaction, resulting in the depletion of any excess surface tin. This results in a low tin chemical potential and Nb_3Sn growth near the tin-poor compositional limit. Specifically, we expect an abrupt change from tin-rich to tin-poor growth at times when the amount of excess tin on the surface drops to zero.

These considerations lead to the following understanding of the composition of vapor diffusion grown Nb_3Sn. Based on experimental measurements, we estimate the amount of excess tin on the Nb_3Sn surface as a function of time during the growth process (Fig. 14) [31,76]. We find that a tin excess is established early on, as the tin chloride nucleation agent evaporates quickly from the source at low temperatures but diffusion and reaction rates on the cavity surface are slow [27]. This ensures a tin-rich growth state early on, which is very important because this early growth ultimately constitutes the

surface of the finished Nb_3Sn layer. This underscores the importance of the nucleation agent: its high vapor pressure at low temperatures, in contrast to the low vapor pressure of the primary tin source, makes it possible to ensure tin-rich initial growth. When this initial excess of tin has been exhausted, we hypothesize that tin-poor growth begins, and tin-poor regions form. At later times, as Nb_3Sn growth slows, the tin deposition rate outpaces the Nb-Sn reaction rate, an excess of tin reappears, and tin-rich growth resumes. Finally, during the annealing step, tin vapor arrival is halted and the remaining surface tin is consumed, resulting in another period of tin-poor growth.

Therefore, we expect the layer to be characteristically tin rich near the surface and tin poor near the niobium-Nb_3Sn interface, with tin-poor regions in the bulk of the layer, consistent with the experimental findings. We observe that while tin-poor growth occurs at predictable depths, it does not generally form a coherent layer. This is likely a result of inherent inhomogeneities in the surface tin supply and in grain boundary diffusion growth.

APPENDIX B: ON THE FORMATION OF TIN-RICH GRAIN BOUNDARIES

Our analysis of Sn_{Nb} antisite defect behavior near grain boundaries improves our understanding how grain boundary segregation can be avoided experimentally. Annealing has been proposed as a way to reliably eliminate tin-rich grain boundaries; this process effectively shifts the equilibrium grain boundary composition from its tin-rich limit of over 30% to its tin-poor limit of less than 20%. But, tin-poor grain boundaries can be even more harmful than tin-rich grain boundaries, in particular because there is no limit to how far tin depletion may extend from the grain boundary given enough time for diffusion to take place. In contrast to the case of bulk Nb_3Sn, where material at the tin-rich phase limit of 26% tin has excellent superconducting properties, neither the tin-rich phase limit nor the tin-poor phase limit is favorable for grain boundaries, making it more difficult to optimize their composition. To do so is necessarily a matter of timing and kinetics: the annealing process should ideally be halted by cooling down the cavity when the average grain boundary is close to 25% tin.

Diffusion on niobium sites, where tin antisite defects are eliminated during annealing, is faster than diffusion on tin sites, where niobium antisite defects begin to form during annealing [43]. This is a happy coincidence that may increase the margin for error in the delicate annealing process. Additionally, finishing the growth process at a lower temperature before entering the annealing step, e.g., 950 °C instead of 1150 °C, may significantly reduce tin segregation at grain boundaries by reducing magnitude of the attractive interaction between Sn_{Nb} defects and grain boundaries. This effect is illustrated by the significant temperature dependence of the red curves in Fig. 8. By reducing tin segregation and reducing diffusion rates, finishing layer growth at a lower temperature may further increase the margin for error in the timing of the annealing step, and/or reduce possible undesirable variations in composition from one grain boundary to another.

[1] N. D. Mermin, Thermal properties of the inhomogeneous electron gas, Phys. Rev. **137**, A1441 (1965).

[2] N. Marzari, D. Vanderbilt, and M. C. Payne, Ensemble Density-Functional Theory for *Ab Initio* Molecular Dynamics of Metals and Finite-Temperature Insulators, Phys. Rev. Lett. **79**, 1337 (1997).

[3] A. van de Walle and G. Ceder, Automating first-principles phase diagram calculations, J. Phase Equilib. **23**, 348 (2002).

[4] S. P. Ong, L. Wang, B. Kang, and G. Ceder, Li-Fe-P-O$_2$ phase diagram from first principles calculations, Chem. Mater. **20**, 1798 (2008).

[5] K. Otsuka and X. Ren, Physical metallurgy of Ti-Ni-based shape memory alloys, Prog. Mater. Sci. **50**, 511 (2005).

[6] A. Planes and L. Mañosa, Vibrational properties of shape-memory alloys, Solid State Phys. **55**, 159 (2001).

[7] L. Mañosa and A. Planes, Materials with giant mechanocaloric effects: Cooling by strength, Adv. Mater. **29**, 1603607 (2017).

[8] A. van de Walle and G. Ceder, The effect of lattice vibrations on substitutional alloy thermodynamics, Rev. Mod. Phys. **74**, 11 (2002).

[9] S. Kadkhodaei, Q.-J. Hong, and A. van de Walle, Free energy calculation of mechanically unstable but dynamically stabilized bcc titanium, Phys. Rev. B **95**, 064101 (2017).

[10] G. Stewart, Superconductivity in the A15 structure, Physica C (Amsterdam) **514**, 28 (2015).

[11] M. G. Mentink, M. M. Dhalle, D. R. Dietderich, A. Godeke, F. Hellman, and H. H. J. ten Kate, The effects of disorder on the normal state and superconducting properties of Nb$_3$Sn, Supercond. Sci. Technol. **30**, 025006 (2017).

[12] A. Godeke, F. Hellman, H. H. J. ten Kate, and M. G. T. Mentink, Fundamental origin of the large impact of strain on superconducting Nb$_3$Sn, Supercond. Sci. Technol. **31**, 105011 (2018).

[13] B. T. Matthias, T. H. Geballe, S. Geller, and E. Corenzwit, Superconductivity of Nb$_3$Sn, Phys. Rev. **95**, 1435 (1953).

[14] J. E. Kunzler, E. Buehler, F. S. L. Hsu, and J. H. Wernick, Superconductivity in Nb$_3$Sn at High Current Density in a Magnetic Field of 88 Kgauss, Phys. Rev. Lett. **6**, 89 (1961).

[15] H. Hilgenkamp and J. Mannhart, Grain boundaries in high-T$_c$ superconductors, Rev. Mod. Phys. **74**, 485 (2002).

[16] S. E. Babcock and J. L. Vargas, The nature of grain boundaries in the high-T$_c$ superconductors, Annu. Rev. Mater. Sci. **25**, 193 (1995).

[17] A. Gurevich, To use or not to use cool superconductors? Nat. Mater. **10**, 255 (2011).

[18] D. Dimos, P. Chaudhari, and J. Mannhart, Superconducting transport properties of grain boundaries in YBa$_2$Cu$_3$O$_7$ bicrystals, Phys. Rev. B **41**, 4038 (1990).

[19] T. Katase, Y. Ishimaru, A. Tsukamoto, H. Hiramatsu, T. Kamiya, K. Tanabe, and H. Hosono, Advantageous grain boundaries in iron pnictide superconductors, Nat. Commun. **2**, 409 (2011).

[20] J. A. Parrell, M. B. Field, Y. Zhang, and S. Hong, Advances in Nb$_3$Sn strand for fusion and particle accelerator applications, IEEE Trans. Appl. Supercond. **15**, 1200 (2005).

[21] T. Baig, Z. Yao, D. Doll, M. Tomsic, and M. Martens, Conduction cooled magnet design for 1.5 T, 3.0 T and 7.0 T MRI systems, Supercond. Sci. Technol. **27**, 125012 (2014).

[22] R. G. Sharma, *Superconductivity: Basics and Applications to Magnets*, Springer Series in Materials Science (Springer, Cham, 2015).

[23] A. Echarri and M. Spadoni, Superconducting Nb$_3$Sn: A review, Cryogenics **11**, 274 (1971).

[24] X. Xu, A review and rospects for Nb$_3$Sn superconductor development, Supercond. Sci. Technol. **30**, 093001 (2017).

[25] S. Posen, N. Valles, and M. Liepe, Radio Frequency Magnetic Field Limits of Nb and Nb$_3$Sn, Phys. Rev. Lett. **115**, 047001 (2015).

[26] S. Posen, M. Liepe, and D. L. Hall, Proof-of-principle demonstration of Nb$_3$Sn superconducting radiofrequency cavities for high Q$_0$ applications, Appl. Phys. Lett. **106**, 082601 (2015).

[27] D. Hall, New insights into the limitations on the efficiency and achievable gradients in Nb$_3$Sn SRF cavities, Ph.D. thesis, Cornell University, 2017.

[28] S. Posen and M. Liepe, Advances in development of Nb$_3$Sn superconducting radio-frequency cavities, Phys. Rev. Spec. Top.–Accel. Beams **17**, 112001 (2014).

[29] U. Pudasaini, G. V. Eremeev, C. E. Reece, J. Angle, J. Tuggle, and M. J. Kelley, Nb$_3$Sn films for SRF cavities: Genesis and RF properties, *19th International Conference on RF Superconductivity (SRF'19), Dresden, Germany* (JACOW Publishing, Geneva, 2019), pp. 810–817.

[30] S. Posen, B. Tennis, J.-Y. Lee, O. S. Melnychuk, Y. M. Pischalnikov, and D. A. Sergatskov, Nb$_3$Sn at Fermilab: Exploring performance, *19th International Conference on RF Superconductivity (SRF'19), Dresden, Germany* (JACOW Publishing, Geneva, 2019), pp. 818–822.

[31] M. Peiniger, M. Hein, N. Klein, G. Mueller, H. Piel, and P. Thuenus, Work on Nb$_3$Sn cavities at Wuppertal, *Proceedings of The Third Workshop on RF Superconductivity*, edited by K. W. Shepard (Argonne National Laboratory, Illinois, USA, 1987), pp. 503–531.

[32] D. Dew-Hughes, Superconducting A-15 compounds: A review, Cryogenics **15**, 435 (1975).

[33] D. A. Rudman and M. R. Beasley, Microscopic superconducting parameters from tunneling in A15 Nb-Sn, Phys. Rev. B **30**, 2590 (1984).

[34] N. S. Sitaraman, T. A. Arias, D. L. Hall, R. D. Porter, and M. U. Liepe, Tin starved pseudo-phase in superconducting thin film Nb$_3$Sn: a DFT and Monte Carlo study, APS March Meeting 2018, Bull. Am. Phys. Soc. (2018).

[35] N. S. Sitaraman, T. A. Arias, P. D. Cueva, M. M. Kelley, R. D. Porter, Z. Sun, M. U. Liepe, D. A. Muller, J. Carlson, A. R. Pack, and M. K. Transtrum, *Ab initio* calculations on the growth and superconducting properties of Nb$_3$Sn, *19th International Conference on RF Superconductivity (SRF'19), Dresden, Germany* (JACOW Publishing, Geneva, 2019), pp. 39–43.

[36] J. Lee, S. Posen, Z. Mao, Y. Trenikhina, K. He, D. L. Hall, M. Liepe, and D. N. Seidman, Atomic-scale analyses of Nb$_3$Sn on Nb prepared by vapor diffusion for superconducting radiofrequency cavity applications: A correlative study, Supercond. Sci. Technol. **32**, 024001 (2019).

[37] J. Lee, Z. Mao, K. He, Z. H. Sung, T. Spina, S. I. Baik, D. L. Hall, M. Liepe, D. N. Seidman, and S. Posen, Grain-boundary structure and segregation in Nb$_3$Sn coatings on Nb for high-performance superconducting radiofrequency cavity applications, Acta Mater. **188**, 155 (2020).

[38] M. C. Payne, M. P. Teter, D. C. Allan, T. A. Arias, and J. D. Joannopoulos, Iterative minimization techniques for *Ab initio* total-energy calculations: Molecular dynamics and conjugate gradients, Rev. Mod. Phys. **64**, 1045 (1992).

[39] R. Sundararaman, K. Letchworth-Weaver, K. A. Schwarz, D. Gunceler, Y. Ozhabes, and T. A. Arias, JDFTx: Software for joint density-functional theory, SoftwareX **6**, 278 (2017).

[40] J. P. Perdew, K. Burke, and M. Ernzerhof, Generalized Gradient Approximation Made Simple, Phys. Rev. Lett. **77**, 3865 (1996).

[41] K. F. Garrity, J. W. Bennett, K. M. Rabe, and D. Vanderbilt, Pseudopotentials for high-throughput DFT calculations, Comput. Mater. Sci. **81**, 446 (2014).

[42] N. Marzari, D. Vanderbilt, A. De Vita, and M. C. Payne, Thermal Contraction and Disordering of the Al(110) Surface, Phys. Rev. Lett. **82**, 3296 (1999).

[43] R. Besson, S. Guyot, and A. Legris, Atomic-scale study of diffusion in A15 Nb_3Sn, Phys. Rev. B **75**, 054105 (2007).

[44] R. Flükiger, T. Spina, F. Cerutti, A. Ballarino, C. Scheuerlein, L. Bottura, Y. Zubavichus, A. Ryazanov, R. D. Svetogovov, S. Shavkin, P. Degtyarenko, Y. Semenov, C. Senatore, and R. Cerny, Variation of T_c, lattice parameter and atomic ordering in Nb_3Sn platelets irradiated with 12 MeV protons: correlation with the number of induced frenkel defects, Supercond. Sci. Technol. **30**, 054003 (2017).

[45] M. Suenaga, D. O. Welch, R. L. Sabatini, O. F. Kammerer, and S. Okuda, Superconducting critical temperatures, critical magnetic fields, lattice parameters, and chemical compositions of "bulk" pure and alloyed Nb_3Sn produced by the bronze process, J. Appl. Phys. **59**, 840 (1986).

[46] B. Fultz, Vibrational thermodynamics of materials, Prog. Mater. Sci. **55**, 247 (2010).

[47] H. M. Tütüncü, G. P. Srivastava, S. Bağcı, and S. Duman, Theoretical examination of whether phonon dispersion in Nb_3Sn is anomalous, Phys. Rev. B **74**, 212506 (2006).

[48] R. Flükiger, R. Isernhagen, W. Goldacker, and W. Specking, Long-range atomic order, crystallographical changes and strain sensitivity of J_c in wires based on Nb_3Sn and other A15 type compounds, Adv. Cryog. Eng. Mater. **30**, 851 (1984).

[49] J. P. Charlesworth, I. Macphail, and P. E. Madsen, Experimental work on the niobium-tin constitution diagram and related studies, J. Mater. Sci. **5**, 580 (1970).

[50] C. Becker, S. Posen, N. Groll, R. Cook, C. M. Schlepütz, D. L. Hall, M. Liepe, M. Pellin, J. Zasadzinski, and T. Proslier, Analysis of Nb_3Sn surface layers for superconducting radio frequency cavity applications, Appl. Phys. Lett. **106**, 082602 (2015).

[51] R. D. Porter, T. Arias, P. Cueva, D. L. Hall, M. Liepe, J. T. Maniscalco, D. A. Muller, and N. Sitaraman, Next generation Nb_3Sn SRF cavities for linear accelerators, *29th Linear Accelerator Conference (LINAC2018), Beijing, China* (JACOW Publishing, Geneva, 2018), pp. 462–465.

[52] D. McLean and A. Maradudin, *Grain Boundaries in Metals* (Clarendon, Oxford, 1957).

[53] C. Toffolon-Masclet, C. Servant, J. Gachon, and B. Sundman, Reassessment of the Nb-Sn system, J. Phase Equilib. **23**, 134 (2002).

[54] A. Godeke, A review of the properties of Nb_3Sn and their variation with A15 composition, morphology and strain state, Supercond. Sci. Technol. **19**, R68 (2006).

[55] R. A. Schiffman and D. M. Bailey, Thermodynamics of the incongruently subliming niobium-tin system, High Temp. Sci. **15:2/3**, 165 (1982).

[56] R. E. Einziger, J. N. Mundy, and H. A. Hoff, Niobium self-diffusion, Phys. Rev. B **17**, 440 (1978).

[57] M. J. R. Sandim, D. Tytko, A. Kostka, P. Choi, S. Awaji, K. Watanabe, and D. Raabe, Grain boundary segregation in a bronze-route Nb_3Sn superconducting wire studied by atom probe tomography, Supercond. Sci. Technol. **26**, 055008 (2013).

[58] P. J. P. Byrne, Superconducting properties from first principles calculations: An ab-initio study of the properties of superconductors under perturbations, Ph.D. thesis, The University of Durham, 2017.

[59] M. M. Kelley, N. S. Sitaraman, and T. A. Arias, *Ab initio* theory of the impact of grain boundaries and substitutional defects on superconducting Nb_3Sn, Supercond. Sci. Technol. **34**, 015015 (2020).

[60] P. Lejček, *Grain Boundary Segregation in Metals* (Springer, Berlin, 2010).

[61] H. Devantay, J. L. Jorda, M. Decroux, J. Muller, and R. Flükiger, The physical and structural properties of superconducting A15-type Nb-Sn alloys, J. Mater. Sci. **16**, 2145 (1981).

[62] G. M. Eliashberg, Interactions between electrons and lattice vibrations in a superconductor, Zh. Eksp. Teor. Fiz. **38**, 966 (1960) [Sov. Phys. JETP **11**, 696 (1960)].

[63] N. Marzari and D. Vanderbilt, Maximally localized generalized Wannier functions for composite energy bands, Phys. Rev. B **56**, 12847 (1997).

[64] A. M. Brown, R. Sundararaman, P. Narang, W. A. Goddard, and H. A. Atwater, Nonradiative plasmon decay and hot carrier dynamics: Effects of phonons, surfaces, and geometry, ACS Nano **10**, 957 (2016).

[65] A. M. Brown, R. Sundararaman, P. Narang, W. A. Goddard, and H. A. Atwater, *Ab initio* phonon coupling and optical response of hot electrons in plasmonic metals, Phys. Rev. B **94**, 075120 (2016).

[66] A. Habib, F. Florio, and R. Sundararaman, Hot carrier dynamics in plasmonic transition metal nitrides, J. Opt. **20**, 064001 (2018).

[67] W. L. McMillan, Transition temperature of strong-coupled superconductors, Phys. Rev. **167**, 331 (1968).

[68] R. Flükiger, *Superconductivity in d- and f-band Metals* (Springer, Berlin, 1982).

[69] J. Carlson, A. Pack, M. K. Transtrum, S. Posen, J. Lee, D. N. Seidman, D. B. Liarte, N. S. Sitaraman, A. Senanian, M. M. Kelley, T. A. Arias, and J. P. Sethna, Analysis of magnetic vortex dissipation in Sn-segregated boundaries in Nb_3Sn superconducting RF cavities, Phys. Rev. B **103**, 024516 (2021).

[70] D. B. Liarte, S. Posen, M. K. Transtrum, G. Catelani, M. Liepe, and J. P. Sethna, Theoretical estimates of maximum fields in superconducting resonant radio frequency cavities: Stability theory, disorder, and laminates, Supercond. Sci. Technol. **30**, 033002 (2017).

[71] A. Sheikhzada and A. Gurevich, Dynamic transition of vortices into phase slips and generation of vortex-antivortex pairs in thin Film Josephson junctions under dc and ac currents, Phys. Rev. B **95**, 214507 (2017).

[72] A. R. Pack, J. Carlson, S. Wadsworth, and M. K. Transtrum, Vortex nucleation in superconductors within time-dependent Ginzburg-Landau theory in two and three dimensions: Role of surface defects and material inhomogeneities, Phys. Rev. B **101**, 144504 (2020).

[73] M. K. Transtrum, G. Catelani, and J. P. Sethna, Superheating field of superconductors within Ginzburg-Landau theory, Phys. Rev. B **83**, 094505 (2011).

[74] M. Suenaga and W. Jansen, Chemical compositions at and near the grain boundaries in bronze-processed superconducting Nb_3Sn, Appl. Phys. Lett. **43**, 791 (1983).

[75] T. Baumgartner, S. Pfeiffer, J. Bernardi, A. Ballarino, and M. Eisterer, Effects of inhomogeneities on pinning force scaling in Nb_3Sn wires, Supercond. Sci. Technol. **31**, 084002 (2018).

[76] S. Posen and D. L. Hall, Nb_3Sn superconducting radiofrequency cavities: Fabrication, results, properties, and prospects, Supercond. Sci. Technol. **30**, 033004 (2017).